Energy 171 (2019) 37–48

Contents lists available at ScienceDirect

Energy

journal homepage: www.elsevier.com/locate/energy

Geometric optimization of two-stage thermoelectric generator using genetic algorithms and thermodynamic analysis

Henan Sun [b], Ya Ge [a], Wei Liu [a], Zhichun Liu [a, b, *]

[a] School of Energy and Power Engineering, Huazhong University of Science and Technology, Wuhan 430074, China
[b] China-EU Institute for Clean and Renewable Energy at Huazhong University of Science and Technology, Wuhan 430074, China

ARTICLE INFO

Article history:
Received 24 September 2018
Received in revised form
19 December 2018
Accepted 1 January 2019
Available online 4 January 2019

Keywords:
Thermoelectric generator
Multi-objective genetic algorithm
Specific power
Entropy generation rate
Exergy destruction rate

ABSTRACT

Multi-objective genetic algorithms are used to optimize the structure, assignment of configuration and load resistance of a two-stage thermoelectric generator, where Skutterudite and Bi_2Te_3 are chosen as upper stage and lower stage TE leg materials, respectively. Heat convection and radiation are considered on the top of the upper substrate. In the optimization process, the specific power and entropy generation rate are considered synchronously as objective functions to maximize the power output per unit area and to minimize the irreversibilities. The FEM is adopted in the simulation model, and the Seebeck effect, together with the Peltier effect, Joule heating, Thomson effect, and Fourier heat conduction phenomena are all considered in the simulation process. Shannon's entropy method is applied to select the best solution from the Pareto Frontier. Besides, the exergy destruction rate is analyzed, the results show that the exergy destruction rate increases as the load resistance increases. In addition, the different relationships between the load resistance and the voltage, power output, efficiency and entropy generation rate are presented. The principle of performance enhancement is also explained by comparing the ZT value along the TE legs. The optimization is important to the development of more compact and high-efficiency thermoelectric generators.

1. Introduction

In recent years, there has been a significant increase in the energy demand, which corresponds to economic development. The development of alternative energy is encouraged because of the limited storage of traditional energy. To solve issues related to energy safety and environmental problems, many countries have focused on solar energy, owing to its clean and renewable characteristics [1]. Apart from solar cells and solar thermal systems, solar thermoelectric generators (TEGs) are considered an alternative technology that can convert heat flux directly into electric power by employing a phenomenon called the Seebeck effect. In despite of its low efficiency, it is mainly used for waste heat recovery systems and power supply systems of space detectors, owing to its long lifespan, small volume, solid-state components, the absence of moving parts, its stable operation, and as well as the absence of pollutant [2].

Because of its comparatively low thermal efficiency, many studies have focused on how to improve the performance of TEGs. The performance can be evaluated by a dimensionless quantity-called the figure of merit (ZT), which is defined as $ZT = \alpha^2\sigma T/\lambda$, where the Seebeck coefficient(α), electrical conductivity(σ) and thermal conductivity(λ) are functions of temperature T.

There are two main ways of improving the performance of TEGs, including making improvements to materials technology. Ways in which this may be realized include employing a sufficiently wider temperature range, a reduction in the thermal conductivity of the lattice, improved thermoelectric properties through doping, removal of impurities, and improved microstructure design [3–10]. Another approach is to optimize the geometric configurations [11]. This paper focuses on the impact of the geometric configuration on the TEG performance as well as on thermodynamic analysis.

G. Fraisse et al. [12] compared the different modeling approaches for thermoelectric coolers (TECs) and TEGs, an overestimation of about 9% at the maximum power point occurred in a standard simplified model, and the finite-element method (FEM) model is the most accurate one in performance prediction. Haider Ali et al. [13] created exponential-shaped TE legs to lower the thermal conductance, they found that the power output and

* Corresponding author. School of Energy and Power Engineering, Huazhong University of Science and Technology, Wuhan 430074, China.
E-mail address: zcliu@hust.edu.cn (Z. Liu).

https://doi.org/10.1016/j.energy.2019.01.003
0360-5442/

thermal efficiency cannot be maximized simultaneously nor can the maximum power output and thermal efficiency be obtained when the dimensionless geometric parameter a = 0. Ge et al. [14] investigated a segmented TEG model using two materials for the hot and cold sides, five parameters (i.e., the current (I), number of TE pairs on the side of the model (N), length of the N- and P- type TE legs at the cold side ($L_{p,c}$, $L_{n,c}$), and area ratio of the legs to a pair (γ)), are optimized simultaneously to obtain the maximum power output and minimum volume using NSGA- II, and the result shows that with an increase in volume, the optimal ratio of hot- and cold-side materials could be obtained to determine the optimum power output. The width of the TE legs and the number of TE pairs on the side should be chosen properly to maximize the use of the TE materials. Jang et al. [15] investigated the effects of the substrate thickness, as well as the length and cross-section of the TE legs on the power output and efficiency, they found that there was a positive correlation between the length of the TE legs and efficiency, cross-sectional ratio, and power output; there was also a negative correlation between the substrate thickness and TEG performance. Meng et al. [16,17] optimized three parameters of a TEG model: the leg length, area ratio, and the number of semiconductor pairs using simplified conjugate gradient algorithm to obtain an optimal power output and efficiency, they found that single-objective optimization can only improve one objective at the expense of reduce another objective which is not desirable. In the TEG model, a weight factor is employed to optimize both the power and conversion efficiency. Ming et al. [18] studied the optimum cross-sectional ratio between N-type and P-type legs, adjusted the distribution of the TE legs, and compared the performance (power and efficiency) and performance per unit area between traditional TEGs, dimensional-optimized TEGs, and compact TEGs using numerical simulations. The result showed that a better power density can be achieved by using geometric optimization. Liang et al. [19] investigated the effect of heat transfer coefficient, hot and cold side temperature and the number of total TE legs on a two-stage TEG model, the results shows that the influence of hold side temperature is greater than the cold side, and the heat transfer coefficient has a great influence on TEG's performance up to 400 W/m^2 K. In addition, they also investigated a segmented TEG model in literature [20], they find that the optimal ratio is related to the hot and cold side temperature, and the temperature of the joint point is the same as corresponding temperature at which the ZT values of Bi_2Te_3 and Skutterudite were equal, and the maximum efficiency decrease with the increase of the length of TE legs. Menon et al. [21] designed a novel radial TEG using conducting polymers, where the TE legs are disk-shaped and stacked together with the separators sandwiched between them co-axially; the hot fluid flows through at the center of the disk and natural convection on the cold side. The results showed that radical TEG with the most advanced material, i.e., polymers, produces a power density that is approximately 1000 $\times$ higher than the flat-plate architectures in the same conditions when the temperature difference is 100 K. Based on the experiment and numerical simulation results, Gou et al. [22] found that by increasing the area of the heat sink and its thermal conductivity, the performance can be improved. Niu et al. [23] combined and optimized the exhaust channel of an internal combustion engine with a TEG system, and they found that to realize equilibrium between the heat transfer and pressure drop inside the channel, a middle-sized channel was selected in addition, the performance of the TEG improved after the increasing the number of channels.

Some researchers investigated TEGs from the perspective of thermodynamics. Nuwayhid et al. [24] investigated the influence of the factors such as the Seebeck coefficient, load resistance and thermal conductivity of the TE legs on its irreversibility. The results showed that the entropy generation rate reached to a minimum when the load resistance equals the internal resistance, and the entropy generation rate decreased as the thermal conductance decreased and the Seebeck coefficient increased.

In recent years, new TEG applications have been developed, Wang et al. [25] developed a wearable miniaturized TEG, an open-circuit voltage of 12.5 V/(Kcm^2) and an output power of 0.026×10^{-6} W/(K^2 cm^2) can be achieved in this miniaturized TE model. Ding et al. [26] combined a solar pond and TEG, taking full advantage of the temperature difference in the water between the top and bottom of the pond. A transient model was built to investigate the optimum performance in different climates. Al-Nimr [27] designed a hybrid solar thermal collector using TEG system that can provide both electric power and hot water. The TEG modules are pipe-shaped with an aperture on the top that allows solar radiation to enter, and cold water passes outside the pipe as a heat sink, while being heated simultaneously. An energy conversion efficiency of 84.5% can be achieved when the solar heat flux density is 1000 W/m^2 and the mass flow rate equals 0.01 kg/s.

However, the study on how to obtain a higher performance per unit area while minimizing the irreversibility of the TEG needs further investigated. The motivation of present study is based on following aspects: 1) The geometry of two-stage TEGs plays an important role in performance, which needs a further optimization. 2) By combining the multi-objective algorithm and the decision making approach, the most compromised solution between the two objectives can be determined to achieve a balance of specific power and entropy generation rate. 3) Exergy destruction rate first discussed in a thermoelectric generator model as a criterion for irreversible heat transfer. This study combines a solar concentrating system with a two-stage cylindrical thermoelectric pair. A precise three-dimensional (3D) model was established by COMSOL Multiphysics and the Seebeck effect, Peltier effect, Thomson effect, Joule heating and Fourier heat conduction phenomena are considered simultaneously [11]. To optimize both the specific power (P') and entropy generation rate ($\dot{S}_{gen}$), multi-objective genetic algorithm was utilized. Five variables were evaluated simultaneously to determine the ideal performance respectively are N/P cross-section ratio of upper stage (γ_1) and lower stage (γ_2), the height of lower stage TE legs (H_L), load resistance (R_L) and the angle between N and P type TE legs (θ). An ideal solution is selected based on the maximum specific power, a Nadir solution is selected based on the minimum entropy generation rate, and a Shannon solution is selected to compromise both objectives from the Pareto front. Temperature distribution along TE legs and performances are compared and studied in detail between initial TEG and optimized one.

2. Modeling

2.1. Two-stage TEG model

A concentrating system is used in combination with the TEG to obtain a higher heat flux on the upper substrate. The solar radiation (Q_{solar}) obtained by the concentrating system is 835 W/m^2, and the solar concentration ratio (C) and optical efficiency (η_{opt}) are 200 and 0.65 respectively. So the heat flux density received by upper substrate Q_{re} ($Q_{re} = C \cdot \eta_{opt} \cdot Q_{solar}$) is 108550 W/m^2.

The schematic diagram of the overall two-stage TEG is shown in Fig. 1. The overall model consists of 18 uni-couples for the in-line arrangement (i.e. $\theta = 90^\circ$). Because they all work under the same operating conditions, only a single uni-couple is optimized in this paper.

Fig. 2 shows the geometric construction of the initial uni-couple. It consists of four cylindrical TE legs, three electrical isolated Al_2O_3

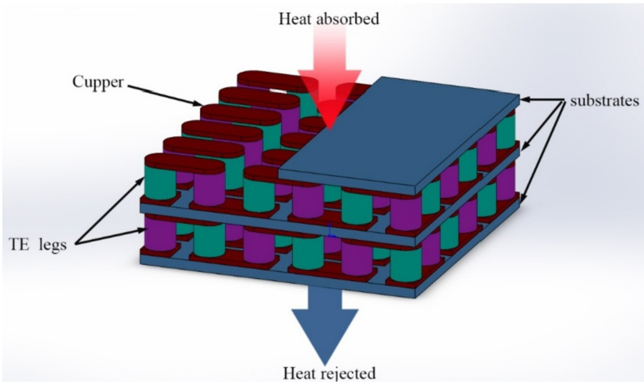

Fig. 1. Schematic diagram of a two-stage TEG module.

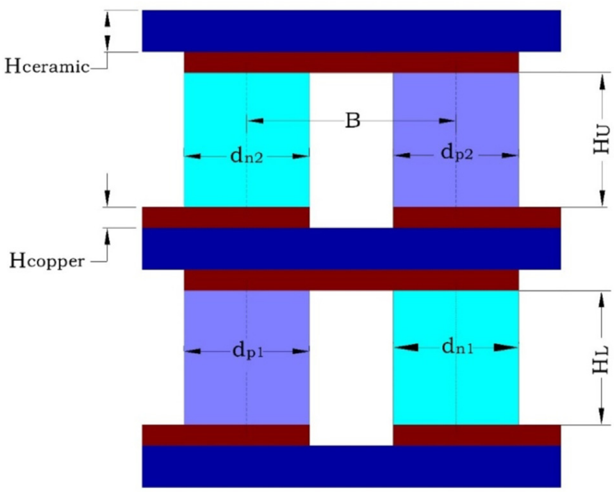

Fig. 2. Geometry construction of an uni-couple.

ceramic and six copper interconnectors. The upper and lower stages are connected in series. Skutterudites was adopted for the upper stage and Bi_2Te_3 for the lower stage; the temperature-dependent material properties of TE legs are shown in Table 1 and Fig. 3.

The area of the substrates is $L_{sub} \times W_{sub} = 14 \times 14 = 196\ mm^2$, where L_{sub} and W_{sub} are length and width of total substrate. The total height of lower and upper stage TE legs (H) is 3.2 mm. And in an uni-couple, the total cross-section area of P- and N-type TE legs (A_{sec}) is 3.5343 mm^2. Therefore for a TEG model, the total volume of thermoelectric material is constant. The height of the lower TE legs $H_L = 1.6$ mm, the diameter of the cylinder $d_{n1} = d_{n2} = d_{p1} = d_{p2} = 1.5$ mm, the distance between the N and P TE legs (B) is 2.5 mm. The load resistance $R_L = 0.072\ \Omega$, which is equal to the internal resistance of the uni-couple. All of the geometric parameters can be deduced after five variables are determined according to Table 2.

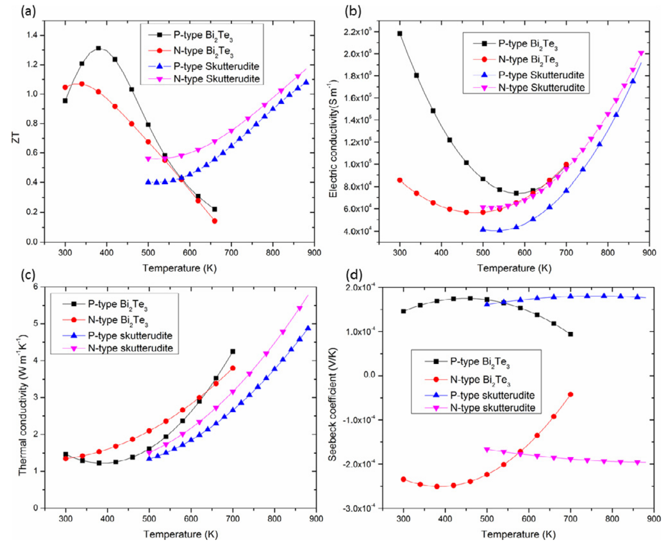

Fig. 3. Temperature dependent TE properties of n-type and p-type Skutterudites as upper stage material, n-type and p-type Bi_2Te_3 as the lower stage material: (a) ZT value, (b) electrical conductivity, (c) thermal conductivity, and (d) Seebeck coefficient.

Table 2
Geometric parameters of initial uni-couple.

Parameter	Value	Unit
Thickness of the substrate ($H_{ceramic}$)	0.5	mm
Thickness of interconnector (H_{copper})	0.25	mm
Total height of TE legs (H)	3.2	mm
Total cross-sectional area (A_{sec})	3.5343	mm^2
Height of lower stage TE legs (H_L)	1.6	mm
Total number of uni-couples (N)	18	1
Diameter of N-type TE leg in lower stage (d_{n2})	1.5	mm
Diameter of P-type TE leg in lower stage (d_{p2})	$\sqrt{\frac{4\cdot(A_{sec}-0.25\pi d_{n2}^2)}{\pi}}$	mm
Diameter of N-type TE leg in upper stage (d_{n1})	1.5	mm
Diameter of P type TE leg in upper stage (d_{p1})	$\sqrt{\frac{4\cdot(A_{sec}-0.25\pi d_{n1}^2)}{\pi}}$	mm
Distance between N- and P-type TE leg (B)	2.5	mm
Length of total substrate (L_{sub})	$B(5+cos\theta)+d_{n1}$	mm
Width of total substrate (W_{sub})	$5Bsin\theta+d_{p1}$	mm
Substrate area of single uni-couple (A_{sub})	$L_{sub}\times W_{sub}/N$	mm^2
Variables	**Value**	**Unit**
N/P cross-sectional ratio of upper stage	$\gamma_1 = (d_{n1}/d_{p1})^2$	1
N/P cross-sectional ratio of lower stage	$\gamma_2 = (d_{n2}/d_{p2})^2$	1
Angle between N- and P- type TE legs	θ	°
Height of lower-stage TE legs	H_L	mm
Load resistance	R_L	Ω

In order to clarify the importance and effectiveness of applying different thermoelectric materials in different temperature ranges, a Skutterudite model, which means that Skutterudite is used for both upper and lower stage thermoelectric legs and has the same structure with Ideal model, Nadir model and Shannon model, is used to compare the performance.

Table 1
The temperature-dependent material properties of TE legs.

Material	Thermal conductivity [$Wm^{-1}K^{-1}$]	Electrical conductivity [S/m]	Seebeck coefficient [V/K]
n-Sku	$1.65\times10^{-5}T^2$-0.01154 T + 3.15454	$1.08586T^2$-1131.212 T + 355392.95	$1.86\times10^{-10}T^2$-3.34×10^{-7}-4.58×10^{-5}
p-Sku	$1.50\times10^{-5}T^2$-0.01138 T + 3.2729	$1.23316T^2$-1306.01 T + 386050.87	$-3.13\times10^{-10}T^2$+4.82×10^{-7}-5.1764×10^{-6}
n-Bi_2Te_3	$1.19\times10^{-5}T^2$-0.00577 T + 2.00418	$0.89631T^2$-860.754 T + 262853.95	$2.31\times10^{-9}T^2$-1.65×10^{-6}T+6.89×10^{-5}
p-Bi_2Te_3	$3.11\times10^{-5}T^2$-0.02413 T + 5.90208	$1.80184T^2$-2101.88 T + 686731.77	$-1.30\times10^{-10}T^2$+1.17×10^{-6}T-8.80×10^{-5}

The concentration system can increase the heat flux of sunlight by a factor of several tens so that the upper substrate can obtain a higher temperature. The temperature difference between two sides of the TE legs drives the current carriers to the cold end, and sequentially generates the electromotive force and the rest of the heat rejects to the heat sink.

2.2. Governing equation

For a steady state TEG, the energy conversion equation and current continuity equation can be written as follows:

$$\nabla \cdot \vec{q} = Q \tag{1}$$

$$\nabla \cdot \vec{j} = 0 \tag{2}$$

where $\vec{q}$ is the heat flux, Q is the Joule heat generated by the TEG, and $\vec{j}$ is the current density, Eqs. (3)–(5) are the definitions of $\vec{q}$, Q, and $\vec{j}$ [14]:

$$\vec{q} = -\lambda \nabla T + \alpha T \vec{j} \tag{3}$$

$$Q = -\nabla V \cdot \vec{j} \tag{4}$$

$$\vec{j} = -\sigma(\nabla V + \alpha \nabla T) \tag{5}$$

In Eq. (3), λ is the thermal conductivity, α is the Seebeck coefficient, the first term on the right side of the equation represents the Fourier heat conduction, and the second term is the Peltier effect. In Eq. (4), V is the electric potential, while in Eq. (5), the first term on the right side represents Ohm's law and the second term represents the Seebeck effect. Eq. (6) is the integration of these five equations:

$$T \nabla \alpha \vec{j} = \nabla \cdot (\lambda \nabla T) + \vec{j} \cdot \left(\sigma^{-1} \vec{j}\right) \tag{6}$$

This means that the TEG transforms heat from the hot junction into electric energy and the rest of the heat is rejected to the cold junction.

2.3. Boundary conditions

To better model an actual situation and to simplify the optimization process, the following assumptions are made in this paper.

(1) The TEG model works in a stable state and the current density is uniform across the section of the material; the temperature and the heat flow are continuous between the interconnectors and the semiconductors.
(2) The thermal insulation materials are padded between the TE legs in an actual TEG system. Therefore, the cylindrical surfaces of the TE legs are assumed to be adiabatic.
(3) There is a natural convection heat transfer and radiation heat transfer on the top surface of the upper substrate. Because the convective heat transfer coefficient (h, W/m^2 K) varies with temperature, it can be obtained via an empirical equation in the uniform heat flux condition (Fig. 4(a)shows the h-T diagram):

$$\mathrm{Nu} = \frac{hl}{\lambda} = 1.076 \times (\mathrm{Gr} \cdot \mathrm{Pr})^{1/6} \tag{7}$$

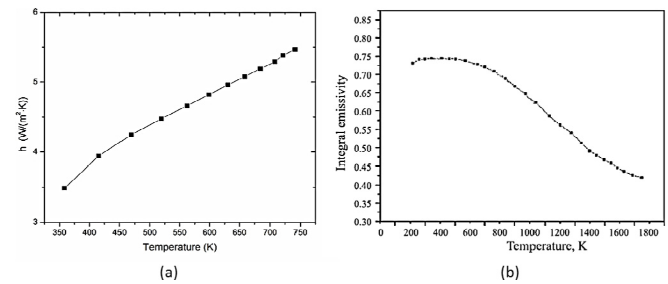

Fig. 4. (a) Variation of convective heat transfer coefficient with temperature (b) Variation of integral emissivity of aluminum oxide ceramics with temperature.

$$Gr^* = Gr \cdot \mathrm{Nu} = \frac{g \alpha_V q L^4}{\lambda \nu^2} \tag{8}$$

where g is the gravitational acceleration; α_V is the coefficient of volume change, L is the characteristic length; ν is the kinematic viscosity, which is equal to 15.06×10^{-6} m^2/s; q is the heat flux; λ is the heat conductivity coefficient of the air, which is equal to 2.59×10^{-2} W m^{-1} K^{-1}. By combining Eq. (7) and Eq. (8), h can be expressed as Eq. (9):

$$h = 5.51 \times (q \times \alpha_V(T))^{1/6} \tag{9}$$

The radiant emissivity of aluminum oxide ceramics is also temperature sensitive, and the relationship between the temperature and emissivity is shown in Fig. 4(b) [28].

(4) The material properties of copper and ceramics are temperature independent. For copper, $\sigma = 5.998 \times 10^7$ S m^{-1} and $\lambda = 400$ W m^{-1} K^{-1} while for ceramics, $\sigma = 1 \times 10^{-14}$ S m^{-1} and $\lambda = 24$ W m^{-1} K^{-1}.
(5) The temperature on the bottom of the upper stage is the same as the temperature on the top of the lower stage.
(6) The sunlight that is focused by the concentration system radiates evenly on the upper substrate, which means that all uni-couples in the system operate under the same boundary conditions; therefore, one uni-couple was used to calculate to reduce the computing resource.
(7) The thermal contact resistance and electrical contact resistance of the uni-couple are relatively small, so they can be neglected; the resistance of the external wire resistance can also be neglected.

For thermal boundary conditions, the Dirichlet boundary condition is applied on the cold side with $T_C = 25$ °C, and the Neumann boundary condition is applied on the hot side with $q = 108550$ W/m^2. For electrical boundary conditions, a load resistance R_L is connected with the uni-couple, which $R_L = R$, where R is internal resistance of the uni-couple.

3. Theoretical analysis and optimization

3.1. Thermal and electrical analysis

The solar radiation received by the upper substrate is shown in Eq. (10) as follows,

$$Q_{re} = A_{sub} \times C \times Q_{solar} \times \eta_{opt}, \tag{10}$$

where, coefficient"C" is the solar concentration ratio, which is a parameter of a solar collector. "C" is the ratio of solar heat flux density at a point on the upper substrate to the projected heat flux density at the collector surface. Q_{solar} is solar radiation obtained by concentrating system and η_{opt} is optical efficiency.

The natural convection heat transfer and radiation heat transfer caused by the temperature rise on the upper substrate are shown in Eqs. (11) and (12).

$$Q_{cov} = A_{sub} \times h \times (T_H - T_{air}) \tag{11}$$

$$Q_{rad} = A_{sub} \times \varepsilon\sigma\left(T_H^4 - T_{amb}^4\right) \tag{12}$$

where T_{air} and T_{amb} are equal to 25 °C, ε is the emissivity and σ is the Stefan-Boltzmann constant, $\sigma = 5.67 \times 10^{-8}\ \mathrm{W\,m^{-2}\,K^{-4}}$, and T_H is temperature at the top of the substrate, which can obtain by COMSOL Multiphysics simulation.

The heat flux on the hot and cold junctions of N and P legs are Q_H and Q_C [19], respectively. Then, Q_M represents the heat released from the upper stage to intermediate layer.

$$Q_H = \alpha_1 T_1 I - \frac{1}{2} I^2 R_1 + K_1 (T_1 - T_3) \tag{13}$$

$$Q_C = \alpha_2 T_3 I + \frac{1}{2} I^2 R_2 + K_2 (T_3 - T_2) \tag{14}$$

$$Q_M = \alpha_2 T_3 I - \frac{1}{2} I^2 R_2 + K_2 (T_3 - T_2) \tag{15}$$

Q_H and Q_M can be rewritten as:

$$Q_H = Q_{re} - Q_{cov} - Q_{rad} \tag{16}$$

$$Q_M = \alpha_1 T_3 I + \frac{1}{2} I^2 R_1 + K_1 (T_1 - T_3) \tag{17}$$

T_3 is the temperature of the intermediate layer. Based on Eqs. (15) and (17), T_3 can be expressed as:

$$T_3 = \frac{K_1 T_1 + K_2 T_2 + \frac{1}{2} I^2 R_1 + \frac{1}{2} I^2 R_2}{K_1 + K_2 + \alpha_2 I - \alpha_1 I} \tag{18}$$

R and K [19] are the internal resistance and heat conductivity of the uni-couple, respectively:

$$R = R_1 + R_2 \tag{19}$$

where

$$R_1 = \frac{L_{p1}}{A_{p1}\sigma_{p1}} + \frac{L_{n1}}{A_{n1}\sigma_{n1}} \tag{20}$$

$$R_2 = \frac{L_{p2}}{A_{p2}\sigma_{p2}} + \frac{L_{n2}}{A_{n2}\sigma_{n2}} \tag{21}$$

and

$$K = K_1 + K_2 \tag{22}$$

$$K_1 = \frac{\overline{\lambda_{p1}} A_{p1}}{L_{p1}} + \frac{\overline{\lambda_{n1}} A_{n1}}{L_{n1}} \tag{23}$$

$$K_2 = \frac{\overline{\lambda_{p2}} A_{p2}}{L_{p2}} + \frac{\overline{\lambda_{n2}} A_{n2}}{L_{n2}} \tag{24}$$

T_1 and T_2 are the temperature of the hot junction of upper stage TE legs and the temperature of cold junction of the lower TE legs, respectively. The current of a two-stage uni-couple can be defined as:

$$I = \frac{\alpha_2 (T_3 - T_2) + \alpha_1 (T_1 - T_3)}{R + R_L} \tag{25}$$

The power output, voltage and efficiency of the uni-couple can be described as:

$$P = I^2 R_L \tag{26}$$

$$V = (\alpha_{p1} - \alpha_{n1})(T_1 - T_3) + (\alpha_{p2} - \alpha_{n2})(T_3 - T_2) \tag{27}$$

$$\eta = \frac{P}{Q_H} \tag{28}$$

The physical parameters of the material, α, σ, and λ are as follows [18], and they are all suitable for both the upper stage and the lower stage:

$$\overline{\alpha_p} = \frac{\int_{T_c}^{T_h} \alpha_p(T)dT}{T_h - T_c} \quad \overline{\alpha_n} = \frac{\int_{T_c}^{T_h} \alpha_n(T)dT}{T_h - T_c} \tag{29}$$

$$\alpha = \overline{\alpha_p} - \overline{\alpha_n} \tag{30}$$

$$\overline{\lambda_p} = \frac{\int_{T_c}^{T_h} \lambda_p(T)dT}{T_h - T_c} \quad \overline{\lambda_n} = \frac{\int_{T_c}^{T_h} \lambda_n(T)dT}{T_h - T_c} \tag{31}$$

$$\overline{\sigma_p} = \frac{\int_{T_c}^{T_h} \sigma_p(T)dT}{T_h - T_c} \quad \overline{\sigma_n} = \frac{\int_{T_c}^{T_h} \sigma_n(T)dT}{T_h - T_c} \tag{32}$$

It should be noted that in order to express the physical parameters of upper and lower TE legs in the same public expression, in Eqs. (29) – (32), upper and lower limits of the integral, T_h and T_c, is a universal way of writing for hot and cold junction temperature for both upper stage and lower stage. Which means, for upper stage, T_h equals to T_1,T_c equals to T_3, and for lower stage, T_h equals to T_3,T_c equals to T_2.

3.2. Entropy generation rate in TEG system

The thermodynamic irreversibility is measured by the entropy generation rate ($\dot{S}_{gen}$), and it can be divided into two parts. The first two terms represent the internal irreversibility and because there is a heat loss at the hot side, the last term Q_e is the external heat dumping to the heat sink, and can be described as follows:

$$\dot{S}_{gen} = -\frac{Q_H}{T_H} + \frac{Q_L}{T_L} + Q_e\left(\frac{1}{T_L} - \frac{1}{T_H}\right) \tag{33}$$

where $Q_e = Q_{re}$ - Q_H, T_H and T_C are the temperatures of the heat source and heat sink, respectively.

3.3. Objective functions

In this study, two objectives are optimized. One is the specific power (P', W/m^2), which is of significance to obtaining a higher power output in a limited space. The other is the entropy generation rate ($\dot{S}_{gen}$, W/K), which is a measure of the degree of irreversibility of the system. The two fitness functions are defined as follows:

$$J_1 = \dot{S}_{gen} \text{ and } J_2 = -P' = -\frac{P}{A_{sub}} \quad (34)$$

3.4. Optimization

In this study, we apply the non-dominated sorting genetic algorithm (NSGA-II) [29,30] to optimize both the specific power and entropy generation rate. In addition, the following constraints are applied to five variables:

$0.04\,\Omega \le R_L \le 0.12\,\Omega$
$0.68 \le \gamma_1 \le 1.44$
$0.68 \le \gamma_2 \le 1.44$
$1\text{ mm} \le H_L \le 2.5\text{ mm}$
$41^\circ \le \theta \le 90^\circ$

Except for the above constraints, some extreme situations are unreachable, such as the negative power output ($P < 0$ W) and the temperature of the intermediate layer is out of a reasonable range ($T_3 > 580$ K), which should be eliminated in the optimization process. The optimization process is shown in Fig. 5; the population size and number of generations are 100 and 100, respectively. The Pareto fraction is 0.6.

In this paper, the Shannon's entropy method [31,32] was chosen as the decision-making method, and it is employed to obtain the weight coefficient of each objective. Given that n alternatives and m objectives are in decision matrix M_{ij}, the process of the Shannon's entropy method is as follows.

L_{ij} is the contribution rate of the ith al28ernative in the jth objective:

$$L_{ij} = \frac{F_{ij}}{\sum_{i=1}^{n} F_{ij}}, \quad i = 1,2,\ldots,n, j = 1,2,\ldots,m \quad (35)$$

E_{ij} is the total contribution of all alternatives:

$$E_j = -K \sum_{i=1}^{m} P_{ij} \ln(P_{ij}) \quad (36)$$

where $K = 1/\ln(m)$, deviation degree D_j is:

$$D_j = 1 - E_j \quad (37)$$

The weight coefficient W_j of the jth objective is:

$$W_j = \frac{Dj}{\sum_{i=1}^{m} D_j} \quad (38)$$

Ultimately,

$$R_i = L_{ij} W_j \quad (39)$$

The Shannon entropy method calculates each point of the Pareto front, where the point with the maximum R_i is the desirable solution. The Ideal and Nadir solutions correspond to the maximum and minimum specific power points, respectively.

4. Results and discussion

4.1. Model validation

To verify the validity of the model, a comparison between the analytical results based on Eqs. (19)–(32) and the simulation result for the power output and voltage was made under the first boundary condition. The analytical result is higher than the simulation result owing to the temperature-independence of its material properties, as shown in Fig. (6), the maximum difference

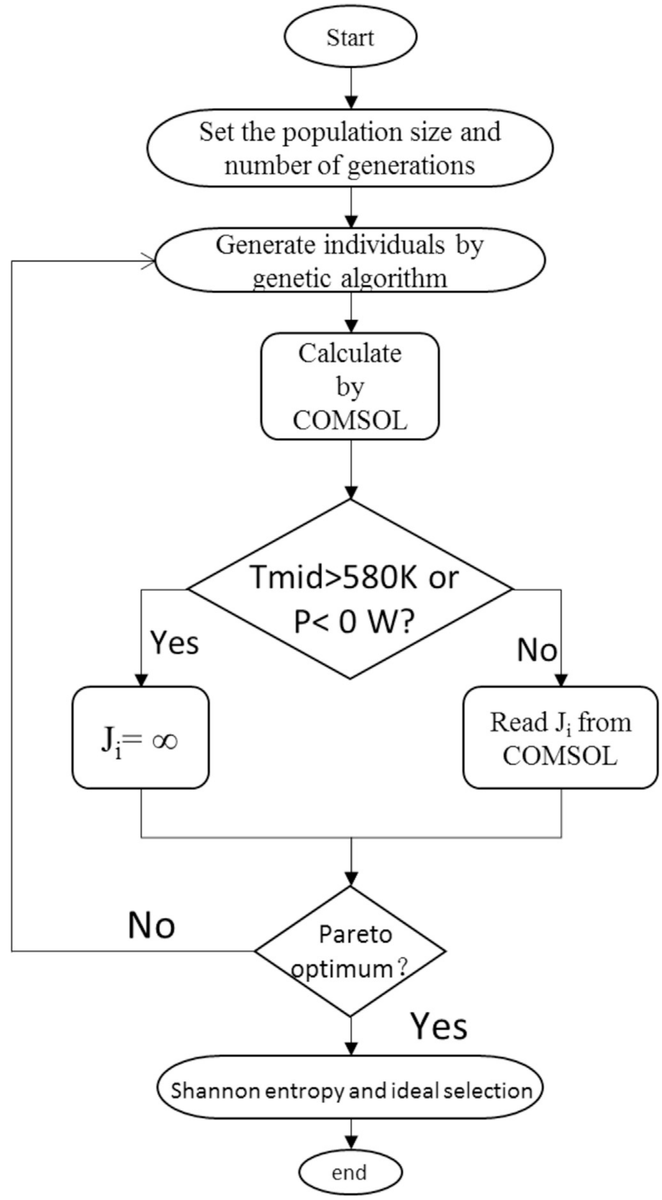

Fig. 5. Flowchart of optimization process.

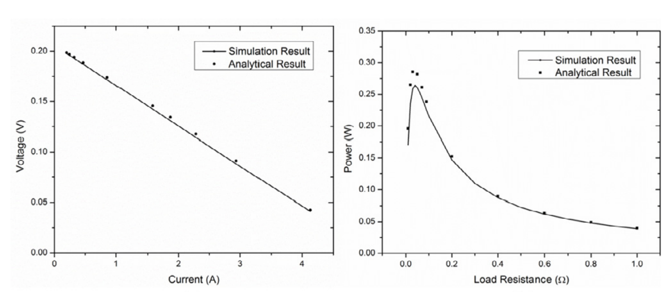

Fig. 6. Comparison of simulation result and analytical result ($T_H = 873.15$ K, $T_C = 303.15$ K, $R_L = 0.072\,\Omega$) (a) Validation of voltage (b) Validation of power.

between simulation voltage and analytical voltage is 3%, while the difference in the maximum power output is 6.35%. The differences are considered to be within reasonable limits according to literature [12]. In addition, a comparison with the results obtains in literature [11] to validate the simulation results. Skutterudite and Bi_2Te_3 are applied for upper and lower stage TE legs. For TE legs on both upper and lower stage, the length is 2 mm and the cross-section area is 2 mm × 2 mm. The geometry parameters and boundary conditions are modified according to literature [11]. As shown in Fig. 7, as the temperature increases, the maximum power difference between two results is less than 4%.

4.2. Optimization results

For the initial model, its load resistance (R_L), N/P cross-sectional ratio of the upper and lower stages (γ_1, γ_2), the height of the lower stage TE legs (H_L), the angle between the N- and P-type TE legs (θ) are 0.072 Ω, 1, 1, 1.6 mm and 90°, respectively.

Fig. 8 is a Pareto front obtain by NSGA-II. The Pareto front is the set of non-dominated solution, where each point represents an optimal solution [33,34]. In this research, the maximum specific power and minimum entropy generation rate is desirable, so two fitness functions in this research, negative specific power on the Y-axis ($-P'$) and entropy generation rate on the X-axis ($\dot{S}_{gen}$), are being optimized. The Pareto front obtained from optimization is curve-shaped, and the specific power increases strictly and monotonically with the entropy generation rate. In addition, we observed that the specific power (P') ranges from 9413.75 W/m^2 to 9850.2 W/m^2 and the entropy generation rate ($\dot{S}_{gen}$) ranges from 8.92×10^{-4} W/K to 1.3×10^{-3} W/K. An ideal solution is selected based on the maximum specific power, a Nadir solution is selected based on the minimum entropy generation rate, and a Shannon solution is selected to compromise both objectives from the Pareto front. The Shannon solution, Ideal solution and Nadir solution are discussed in this paper, and the variables and their performance are listed in Table 3. The cross-sectional profiles of the upper and lower stages of three models are shown in Fig. 9.

The variables at each point of the Pareto front are shown in Figs. 10–13, where the horizontal axis "Individual number" represents the number of the optimal solution, it is calculated as followed: The number of the optimal solution = Pareto fraction × population size. In this research, the Pareto fraction is 0.6, and the population size is 100. So, in Figs. 10–13, the individual number is 60. As can be seen from the graphs, as the specific power and entropy generation rate increase, the N/P cross-sectional ratios of the upper and lower stages are almost constant, γ_1 is about 0.825, while γ_2 is about 1.248. Similarly, the load resistance of the uni-couple is about 0.0687 Ω, which means that the load resistance of the total model consisting of 18 uni-couples is about 1.2366 Ω. However, as the specific power increases, the length of the lower TE legs (H_L) decreases from 2.41 mm to 1.82 mm, and the angle between the N and P legs (θ) increases from 41° to 76°. This is mainly because the larger the angle, the larger the area of the substrate, which causes the increase of the solar radiation received by the upper substrate (q), furthermore, the temperature on the top of the substrate increases as the heat received increases. To obtain a higher power output, the length of the upper TE legs made of Skutterudite increases, which means that H_L decrease accordingly.

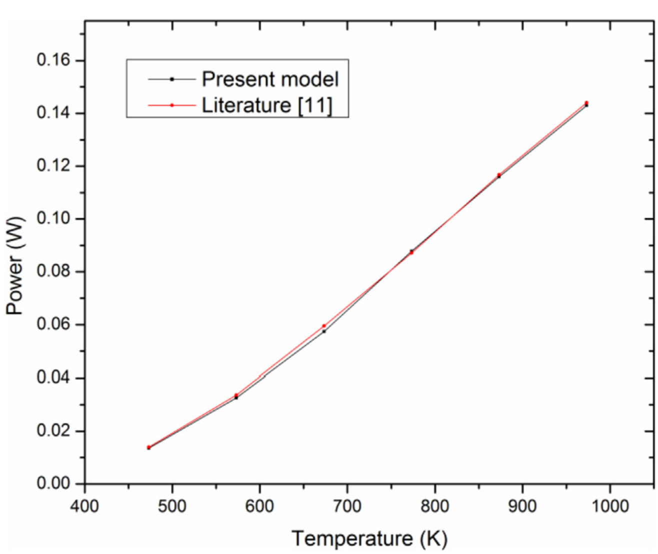

Fig. 7. Comparison of the simulation results with the results in literature [11].

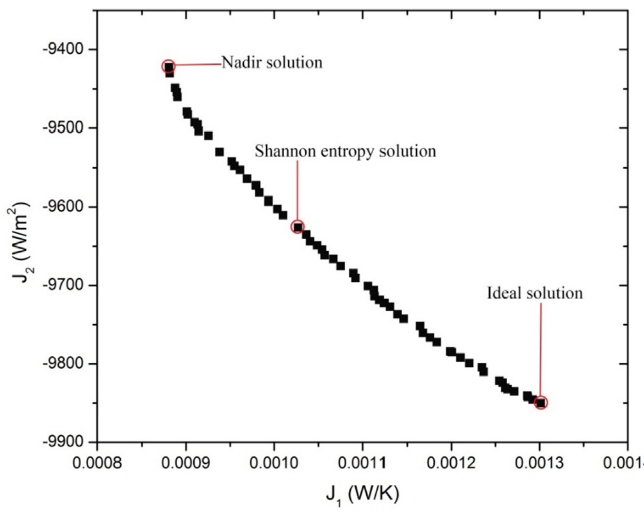

Fig. 8. Pareto front with Shannon solution, Ideal solution and Nadir solution.

4.3. Discussion

Because all 18 uni-couples work under the same conditions, it is obvious that the values of the power, load resistance, voltage, and entropy generation rate of the model are 18 times that of one uni-couple, while the efficiency are the same.

To evaluate the performance of the optimized TEG, Fig. 14 illustrates the ZT distribution along the TE legs of the Ideal model and the Skutterudite model when load resistance of the model is 1.296 Ω. For the lower stage, the ZT value of the Ideal model is greater than that of the Skutterudite model because Bi_2Te_3 has a better performance than Skutterudite when the temperature is below 580 K. For the upper stage, the ZT value of the P-type material of the Ideal model is higher than that of the Skutterudite model. On the contrary, the ZT value of the N-type material of the Skutterudite model is higher than that of the Ideal model. This is mainly because the heat source is under the second boundary condition, which means that although the heat flux density is constant, the temperature on the top of the upper substrate changes as the variables change. For the Skutterudite model, the temperature of the upper stage ranges from 566.77 K to 718.1 K when the load resistance increases from 0.18 Ω to 18 Ω, while for the Ideal model, it ranges from 569.21 K to 693.6 K. This means that the temperature of the Skutterudite model is higher than that of the corresponding position of the Ideal model. The average ZT value of

Table 3
Variables and performances of Shannon, Ideal and Nadir solution.

Variables						Performances	
Solution	R_L (Ω)	γ_1	γ_2	H_L (mm)	θ (°)	P' (W/m^2)	$\dot{S}_{gen}$ (W/K)
Shannon	0.0688	0.846	1.259	2.05	41.95	9630.89	1.05×10^{-3}
Ideal	0.069	0.841	1.169	1.82	49.14	9850.21	1.3×10^{-3}
Nadir	0.0692	0.846	1.259	2.41	77.54	9413.75	8.92×10^{-4}

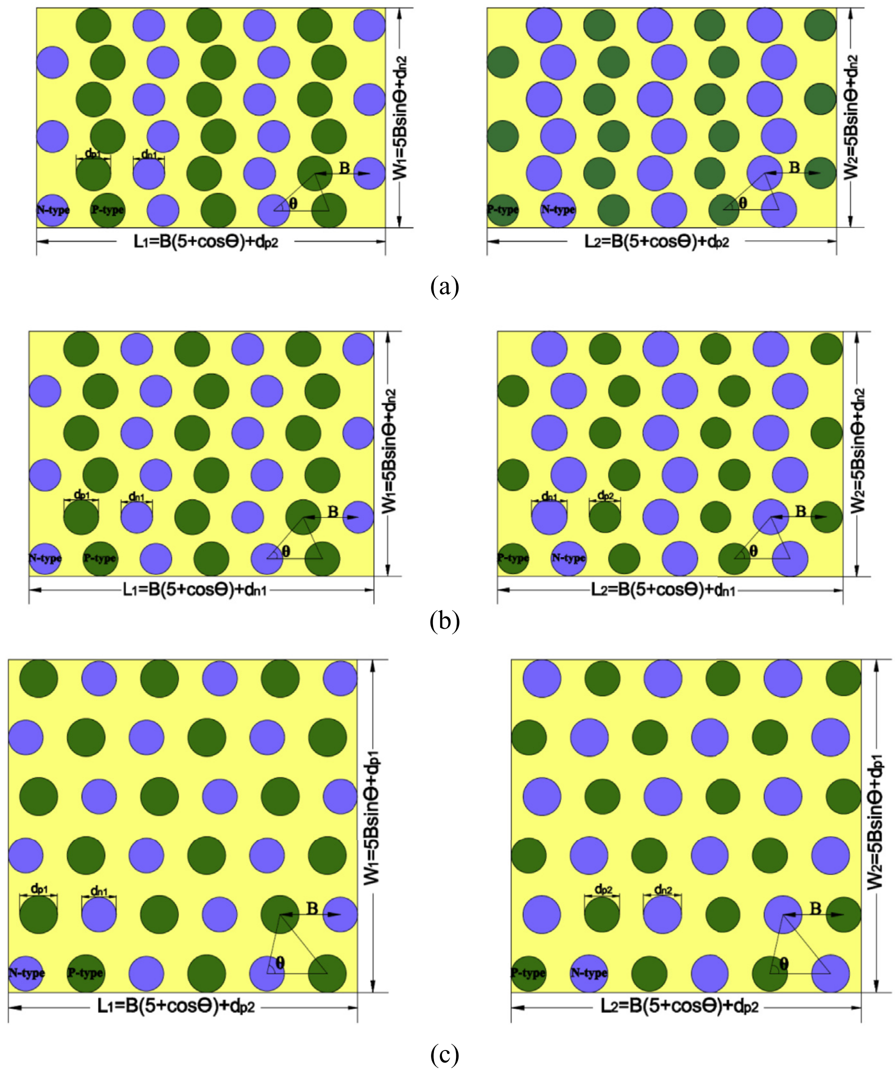

Fig. 9. The cross-sectional profiles of the upper and lower stages of the (a) Shannon model, (b) Ideal model, and (c) Nadir model.

P-type TE legs increases from 0.482 (Skutterudite model) to 0.842 (Ideal model), and that of the N-type TE legs increases from 0.63 (Skutterudite model) to 0.706 (Ideal model).

Figs. 15–16 shows the respective variations of the voltage and power output with the load resistance for different configurations. By comparing the three models, the Ideal model generates the highest voltage and power output among them, while Nadir's the lowest. As the external resistance increases, the voltage first increases sharply, then become slower, and the power output first increases to a maximum value then decreases. At the maximum power point, the material's internal resistance is equal to the load resistance, and the power output of the Ideal, Shannon and Nadir model are respectively 1.96 W, 1.66 W, and 1.49 W. Compared with the Skutterudite model, their increase rate are 36.4%, 15.52%, and 3.69% respectively. Besides, by comparing the Skutterudite and Nadir models, when the load resistance is less than 3.6 Ω, the Nadir model generates more power than the Skutterudite model, but when the load resistance is greater than 3.6Ω, the Skutterudite model generates more power. This is mainly due to the inappropriate material that is applied to the lower stage of the Skutterudite model; as the load resistance increases, the temperature of the hot junction increases and the gradual increase in the power of the upper stage compensates for the poor performance of the lower stage.

Fig. 17 shows the R-η curves, which illustrate the variation in the efficiency with the load resistance for different configurations. The

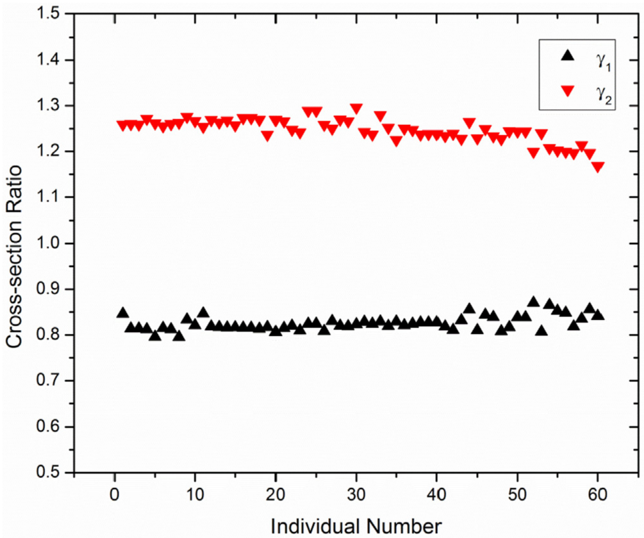

Fig. 10. Variation of the optimal cross-sectional ratio of the upper stage and lower stage.

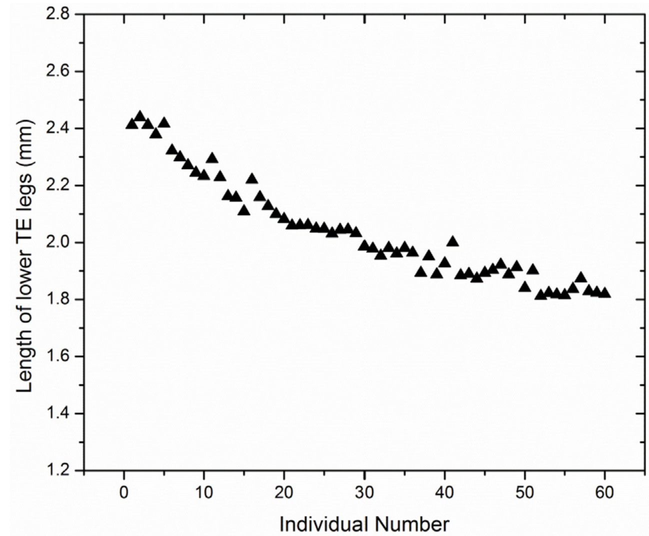

Fig. 12. Variation of the optimal length of lower TE legs.

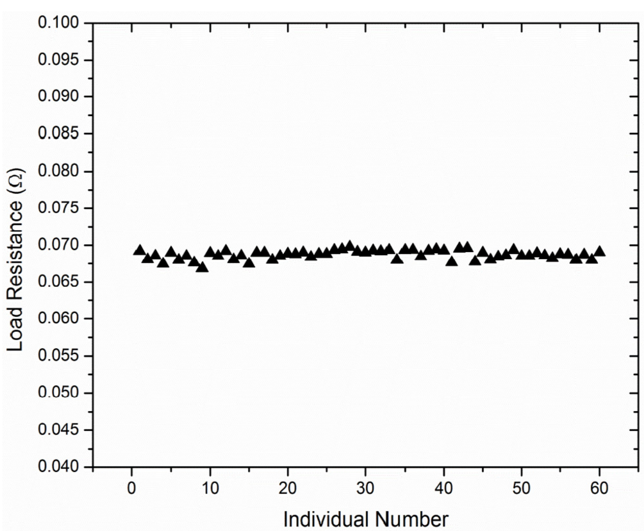

Fig. 11. Variation of the optimal load resistance.

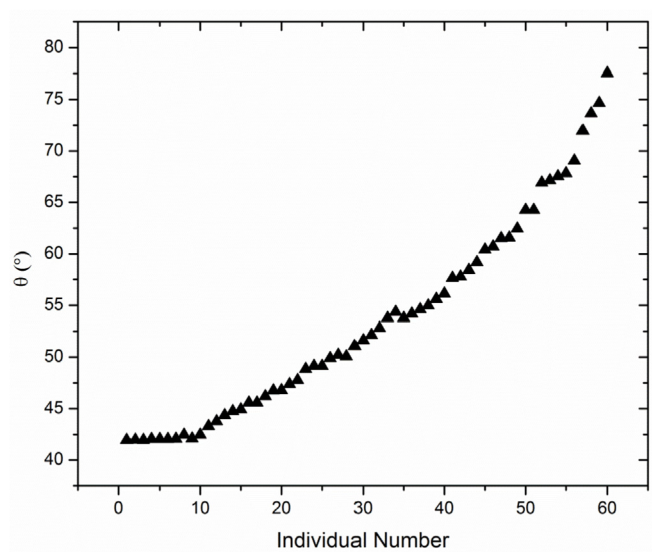

Fig. 13. Variation of the optimal angle between N and P legs.

variation is seen to be similar to that of the power, but it should be noted that the power and efficiency can reach their maximum values simultaneously because the Neumann boundary condition is applied on the hot side. The maximum efficiency of Ideal, Shannon and Nadir models are 10.14%, 9.75%, and 9.48%, respectively; compared with the Skutterudite model, their increase rate are 31.21%, 26.16%, and 22.67% respectively.

Fig. 18 shows the relationship between the entropy generation rate and the load resistance. We can clearly see that as the load resistance increases, the entropy generation rate decreases and then increases gradually. The Skutterudite model produces the largest entropy generation rate followed by the Ideal model, the while Nadir model produces the least. The minimum entropy generation rate of the Ideal, Shannon, and Nadir models are 1.40×10^{-3} W/K, 1.05×10^{-3} W/K, and 9.24×10^{-4} W/K respectively. Compared with the Skutterudite model, the decrease rate of the Ideal, Shannon and Nadir model at the minimum point are 28.77%, 46.51%, and 52.92%, respectively. The conclusions also indicate that when TEGs work under the condition that a large difference occurs between the load resistance and internal resistance, the thermodynamics irreversibility of the TEG is significantly increased.

4.4. Exergy destruction rate analysis

The local exergy destruction rate is deduced based on the analysis of convective heat transfer. Exergy is defined as available energy that can be infinitely converted into any other form of energy, and it is an indicator of the quality of the energy. The local exergy destruction rate can be expressed as [35]:

$$I_{local} = T_0 \frac{\lambda(\nabla T)^2}{T^2} \tag{40}$$

where T_0 is the environmental temperature, λ is the thermal conductivity of the materials, and ∇T is the temperature gradient of

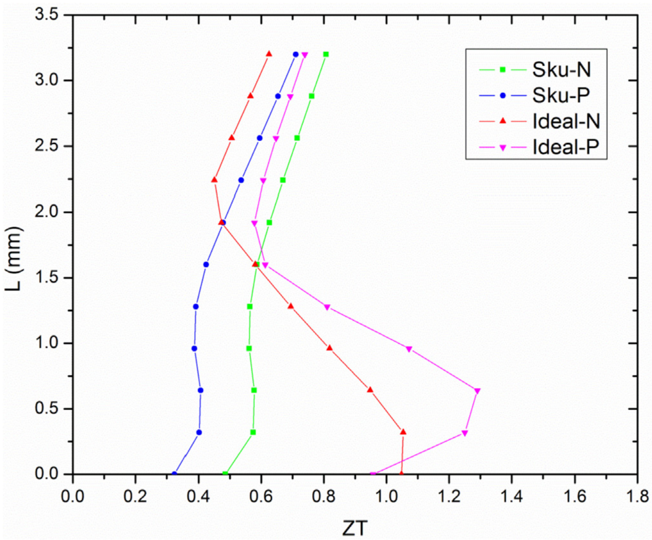

Fig. 14. Distribution of ZT value along TE legs of Skutterudite model and Ideal TEG.

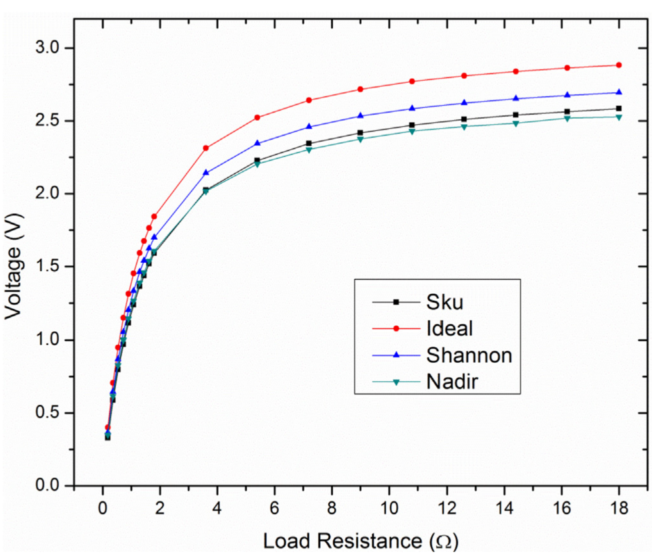

Fig. 15. Variation of voltage with load resistance.

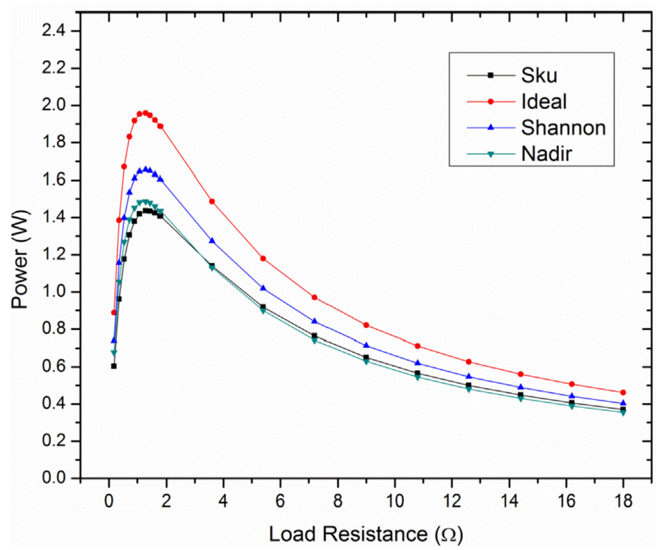

Fig. 16. Variation of power output with load resistance.

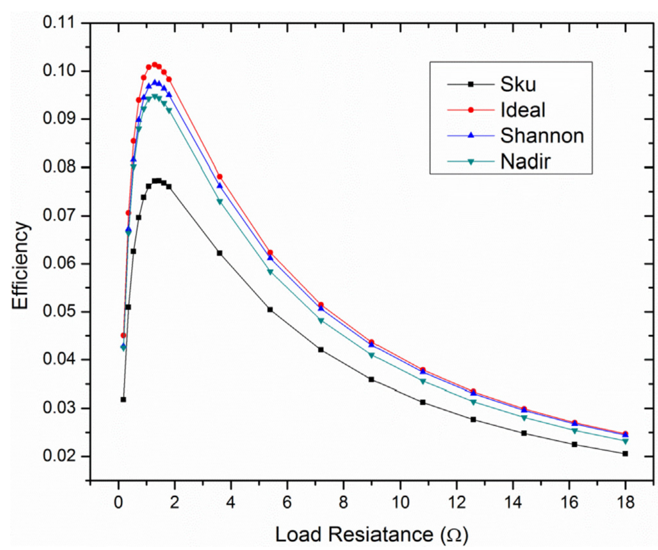

Fig. 17. Variation of efficiency with load resistance.

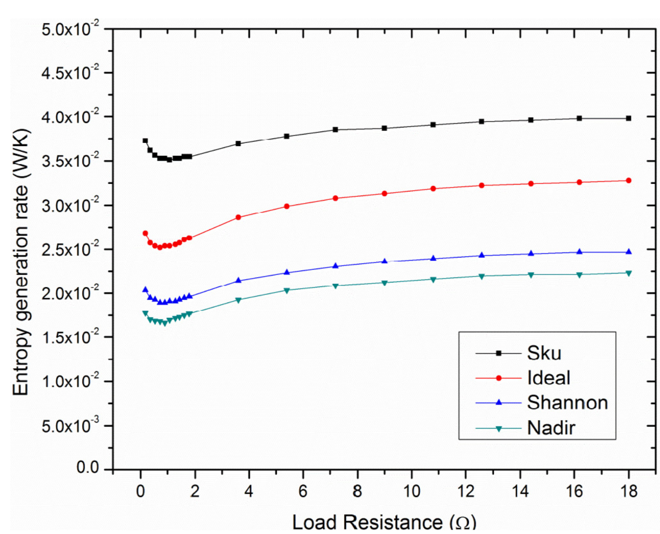

Fig. 18. Variation of entropy generation rate with load resistance.

each point. The total exergy destruction rate of the entire TEG model is:

In Eq. (41), the right hand is the integral of the entire volume of the model. The analysis results in Fig. 19 show that as the load resistance increases, the local exergy destruction rate first grows rapidly then become slower. Then, the Skutterudite model produces the largest local exergy destruction rate, followed by the Ideal model, while the Nadir model produces the least. It should be noticed that the four models in Fig. 19 have same order arrangement as in Fig. 18. For a TEG model, the higher the entropy generation rate, the higher will be the exergy destruction rate. This means that the exergy destruction rate is also a criterion for irreversible heat transfer, and the greater the exergy destruction rate, the greater will be irreversible heat transfer losses in the process.

5. Conclusions

This study employs the NSGA-II in the model optimization, and

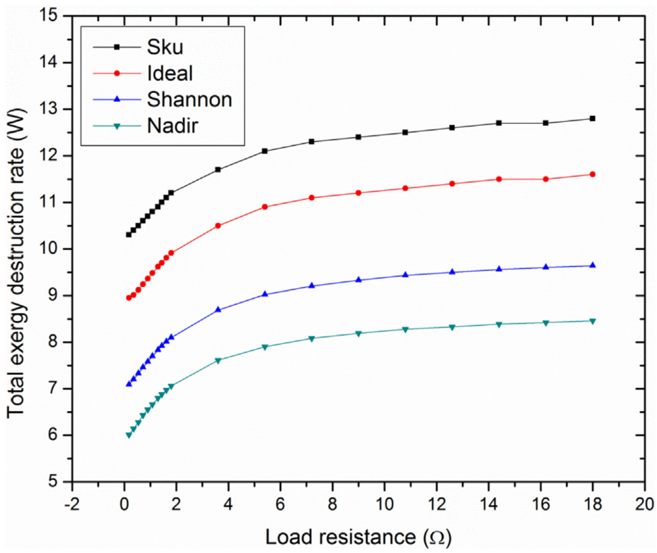

Fig. 19. Variation of total exergy destruction rate of entire model with load resistance.

the maximum specific power and minimum entropy generation rate is considered simultaneously. Shannon's entropy method was chosen as the decision-making method to select a proper solution from the Pareto front, it gives the corresponding weight coefficients to both objectives based on the contribution rate of two objectives. The influence of the load resistance on the voltage, power output, efficiency, entropy generation rate, and exergy destruction rate are predicted; the results obtained for the Skutterudite model, Ideal model, Shannon model and Nadir model are as follows:

1) In the Pareto front, the specific power increases strictly and monotonically with the entropy generation rate. For an optimized TEG, there exists an optimal N/P cross-sectional ration at both the lower stage and upper stage (γ_1,γ_2)as well as a load resistance (R_L) to achieve a maximum specific power; however γ_1,γ_2 and R_L basically remain unchanged in Pareto non-dominated Sorting. For optimal γ_1, γ_2 are approximately 0.825 and 1.248, respectively. And optimal R_L is 1.2366 Ω.
2) With an increase of the angle between the N and P legs (θ), the area of the upper substrate increases. Then, the temperature of the upper substrate increases owing to the greater amount of solar radiation received by the upper substrate. The lengths of the lower TE legs (H_L) decrease to obtain higher power output.
3) A comparison of the Skutterudite model with the three other optimized models shows that replacing Skutterudite by Bi_2Te_3 at the lower stage could improve the ZT value at the same position at the lower stage. However, with respect to the upper stage, there is no significant improvement because the Skutterudite model has a higher temperature at hot junctions.
4) Compared with the Skutterudite model, the power, voltage, and efficiency of the Ideal model and Shannon model are all improved significantly as the load resistance increased. However, for the Nadir model, the voltage and power are lower than the Skutterudite model when the load resistance is greater than 3.6 Ω. The power and efficiency can reach to their maximum simultaneously because the Neumann boundary condition is applied at the hot side.
5) Replacing the lower TE legs from Skutterudite to Bi_2Te_3 can improve the average ZT value of TEG significantly. The ZT value of P type TE legs in the Ideal model is significantly improved compared to the Skutterudite model (from 0.482 to 0.842), while the ZT value of N type TE legs is less improved (from 0.63 to 0.706).
6) The entropy generation rate is an evaluation method for thermodynamic irreversibility. Compared with the Skutterudite model, the entropy generation rate of the three models decreased significantly, especially for the Nadir model, although the Nadir model generates the lowest specific power.
7) The exergy destruction rate is also a criterion for irreversible heat transfer, so the order of the four models for exergy destruction rate is as same as the order with respect to the entropy generation rate. The total exergy destruction rate is the sum of the local exergy destruction rate of each part of the TEG (substrates, interconnectors, and TE legs). In addition, it increases as the load resistance increases.

Based on the above conclusions, it can be summarized that the three optimized models all have better performance than the Skutterudite model, where the Ideal model generates the highest specific power, and the Nadir model produces the smallest entropy generation rate and total exergy destruction rate. Meanwhile, the Shannon model is a compromise solution between the Ideal model and Nadir model. However, it is undesirable to operate the TEG system when the load resistance is much larger or smaller than the internal resistance.

Acknowledgment

The work is supported by the National Natural Science Foundation of China (NOs. 51776079 & 51736004) and the National Key Research and Development Program of China (NO. 2017YFB0603501-3).

Nomenclature

C	Solar concentration ratio
ZT	figure of merit
T	temperature (K)
T_0	environment temperature (K)
T_1	temperature at the top of upper TE legs (K)
T_2	temperature at the bottom of lower TE legs (K)
T_3	temperature of the intermediate layer (K)
T_C	temperature at the cold side (K)
T_H	temperature at the hot side (K)
R_L	load resistance (Ω)
H_L	height of lower stage TE legs (mm)
θ	angle between N and P type TE legs (°)
P	power output (W)
P'	specific power (W/m^2)
$\dot{S}_{gen}$	entropy generation rate (W/K)
J	objective function
d	diameter of cylindrical TE legs (mm)
N	total number of uni-couples
I	electric current (A)
V	electric voltage (V)
I_{local}	local exergy destruction rate (W/m^3)
I_{total}	total exergy destruction rate (W)

Abbreviation

TEG	thermoelectric generator
TEC	thermoelectric cooler

Greek letters

α	Seebeck coefficient (V/K)
λ	thermal conductivity (W/m·K)

σ	electrical conductivity (S/m)
γ	cross-sectional ratio between N and P type

Subscript

1	upper stage
2	lower stage
n	n-type
p	p-type

References

[1] Aaditya AC, Praveen K, Harish CB. Performance evaluation of a natural convective-cooled concentration solar thermoelectric generator coupled with a spectrally selective high temperature absorber coating. Sol Energy Mater Sol Cells 2016;145:333–41.

[2] Sahin AZ, Yilbas BS, Shuja SZ, Momin O. Investigation into topping cycle: thermal efficiency with and without presence of thermoelectric generator. Energy 2011;36(7):4048–54.

[3] Hee SK, Keiko K. Design of segmented thermoelectric generator based on cost-effective and light-weight thermoelectric alloys. Mater Sci Eng B 2014;185: 45–52.

[4] Zhao XB, Ji XH, Zhang YH. Bismuth telluride nanotubes and the effects on the thermoelectric properties of nanotube-containing nanocomposites. Appl Phys Lett 2005;86(6):1665.

[5] Poudel B, Qing H, Ren Z. High-thermoelectric performance of nanostructured bismuth antimony telluride bulk alloys. Science 2008;320(5876):634–8.

[6] Hu LP, Zhu TJ, Liu XH, Zhao X. Point defect engineering of high-performance bismuth-telluride-based thermoelectric materials. Adv Funct Mater 2014;24(33):5211–8.

[7] Biswas K, He J, Blum ID. High-performance bulk thermoelectrics with all-scale hierarchical architectures. Nature 2012;489(7416):414–8.

[8] Wang Y, Rogado NS, Cava RJ. Spin entropy as the likely source of enhanced thermopower in NaxCo2O4. Nature 2003;423(6938):425–8.

[9] Hu Y, Zeng L, Minnich AJ, Dresselhaus MS, Chen G. Spectral mapping of thermal conductivity through nanoscale ballistic transport. Nat Nanotechnol 2015;10:701–6.

[10] Zeng L, Chen G. Disparate quasiballistic heat conduction regimes from periodic heat sources on a substrate. Appl Phys 2014;116(6):539.

[11] Liu ZC, Zhu SP, Ge Y, Liu W. Geometry optimization of two-stage thermoelectric generators using simplified conjugate-gradient method. Appl Energy 2017;190:540–52.

[12] Fraisse G, Ramousse J, Sgorlon D, Goupil C. Comparison of different modeling approaches for thermoelectric elements. Energy Convers Manag 2013;65: 351–6.

[13] Haider A, Ahmet ZS. Thermodynamic analysis of a thermoelectric power generator in relation to geometric configuration device pins. Energy Convers Manag 2014;78:634–40.

[14] Ge Y, Liu ZC, Sun HN, Liu W. Optimal design of a segmented thermoelectric generator based on three-dimensional numerical simulation and multi-objective genetic algorithm. Energy 2018;147:1060–9.

[15] Jang B, Han S, Kim JY. Optimal design for micro-thermoelectric generators using finite element analysis. Microelectron Eng 2011;88:775–8.

[16] Meng JH, Zhang XX, Wang XD. Multi-objective and multi-parameter optimization of a thermoelectric generator module. Energy 2014;71:367–76.

[17] Huang YX, Wang XD, Cheng CH, Lin TW. Geometry optimization of thermoelectric coolers using simplified conjugate-gradient method. Energy 2013;59: 689–97.

[18] Ming TZ, Yang W, Huang X, Wu W, Li X. Analytical and numerical investigation on a new compact thermoelectric generator. Energy Convers Manag 2017;132:261–71.

[19] Liang Xingyu, Sun Xiuxiu, Tian Hua, Shu Gequn, Wang Yuesen, Wang Xu. Comparison and parameter optimization of a two-stage thermoelectric generator using high temperature exhaust of internal combustion engine. Appl Energy 2014;130:190–9.

[20] Tian Hua, Sun Xiuxiu, Qi Jia, Liang Xingyu, Shu Gequn, Wang Xu. Comparison and parameter optimization of a segmented thermoelectric generator by using the high temperature exhaust of a diesel engine. Energy 2015;84:121–30.

[21] Menon AK, Yee SK. Design of a polymer thermoelectric generator using radial architecture. J Appl Phys 2016;119(5):1457–61.

[22] Gou XL, Xiao H, Yang S. Modeling, experimental study and optimization on low-temperature waste heat thermoelectric generator system. Appl Energy 2010;87(10):3131–6.

[23] Niu ZQ, Diao H, Yu S, Jiao K, Du Q. Investigation and design optimization of exhaust-based thermoelectric generator system for internal combustion engine. Energy Convers Manag 2014;85:85–101.

[24] Nuwayhid RY, Moukalled F, Noueihed N. On entropy generation in thermoelectric devices. Energy Convers Manag 2000;41(9):891–914.

[25] Wang ZY, Vladimir L, Paolo F, Chris VH. Realization of a wearable miniaturized thermoelectric generator for human body applications. Sensor Actuator Phys 2009;156(1):95–102.

[26] Ding LC, Akbarzadeh A, Date A, Henrik L, Mark JK. Transient model to predict the performance of thermoelectric generators coupled with solar pond. Energy 2016;103:271–89.

[27] Al-Nimr MA, Al-Darawsheh IA, Al-Khalayleh LA. A novel hybrid cavity solar thermal collector. Renew Energy 2018;115:299–307.

[28] Mironov RA, Zabezhailov MO, Borodai SP. Theoretical-experimental determination of the temperature dependence of the integral emissivity of an alumina ceramic. Refract Ind Ceram 2015;1:424–7.

[29] Deb K, Pratap A, Agarwal S, Meyarivan T. A fast and elitist multiobjective genetic algorithm: NSGA-II. Evol Comput IEEE Trans 2002;6:182–97. https://doi.org/10.1109/4235. 996017.

[30] Ge Ya, Shan Feng, Liu Zhichun, et al. Optimal structural design of a heat sink with laminar single-phase flow using computational fluid dynamics-based multi-objective genetic algorithm. J Heat Trans Transac ASME 2017;140(2): 022803–9.

[31] Shi YJ, Sun GH, Jing J, Dong SH. Shannon and Fisher entropy measures for a parity-restricted harmonic oscillator. Laser Phys 2017, 125201.

[32] Ranjana A, Kaushik Rajesh A. Thermodynamic modeling and multi-objective optimization of two stage thermoelectric generator in electrically series and parallel configuration. Appl Therm Eng 2016;103:1312–23.

[33] Ge Ya, Liu Zhichun, Liu Wei. Multi-objective genetic optimization of the heat transfer for tube inserted with porous media. Int J Heat Mass Tran 2016;101: 981–7.

[34] Ge Y, Wang SC, Liu ZC, et al. Optimal shape design of a minichannel heat sink applying multi-objective optimization algorithm and three-dimensional numerical method. Appl Therm Eng 2019;148:120–8.

[35] Wang JB, Liu W, Liu ZC. The application of exergy destruction minimization in convective heat transfer optimization. Appl Therm Eng 2015;88:384–91.